Anomalous water absorption in cement-based materials caused by drying shrinkage induced microcracks

Z. Wu [1, 2], H.S. Wong [1]*, C. Chen [1] and N.R. Buenfeld [1]

[1] Department of Civil and Environmental Engineering, Imperial College London, SW7 2AZ, UK

[2] Aplustopia Science Research Institute, Canada

Abstract

This paper concerns understanding the influence of drying induced microcracking on water absorption by capillary suction. Paste, mortar and concrete samples with different binder type, w/b ratio, thickness, aggregate size, and curing age were tested. Samples were subjected to gentle stepwise drying at 21°C / 93% → 55% RH, or drying at 21°C / 55% RH, 21°C / 0% RH, 50°C or 105°C to induce microcracks less than 100 μm wide. Results show that the presence of microcracks causes cumulative water absorption to scale non-linearly with $\sqrt{t}$. The observed relationship is approximately sigmoidal / *S*-shaped, with the position of inflection point related to microcracking and the degree of non-linearity increasing with drying severity. A simple fluorescence imaging method was developed to enable continuous monitoring of the advancing wetting front and to study the effect of microcracks. Quantitative image analysis of water penetration produced results consistent with gravimetric measurements.

Keywords: Drying shrinkage (C); Microcracks (B); Transport properties (C); Durability (C); Sorptivity; Anomalous absorption.

1. Introduction

Most concrete structures in service experience drying and wetting cycles and are rarely saturated. Examples include all unsheltered structures, basements and foundations that experience fluctuating groundwater, and parts of marine and coastal structures subjected to tidal zone or salt spray. In such exposure environments, the rate of ingress of water and the accumulation of dissolved aggressive species into partially saturated concrete are largely controlled by capillary absorption rather than Fickian diffusion or pressure-induced flow. Therefore, flow driven by capillary suction is a major transport process that influences the long-term durability of many concrete structures.

Laboratory-based transport testing has been carried out for many years to gain a better understanding of factors that influence capillary transport. The most widely adopted method is the capillary rise method described in BS EN 13057 [1], BS EN 1015-18 [2], BS EN ISO 15148:2002 [3], NT Build 368 [4] and ASTM C1585 [5]. This is also known as the "sorptivity" test based on that developed by Hall [6]. The test exposes one surface of a pre-dried sample to water and measures the increase in mass resulting from absorption as a function of time. The cumulative water absorbed is proportional to the square-root of time ($\sqrt{t}$) and the rate of absorption, defined as sorptivity, is obtained from the slope of this linear relationship. The sorptivity relates to microstructure and initial moisture content and is therefore influenced by mix composition, degree of hydration and exposure conditions. It is also an easily measured property, yet rigorously defined in unsaturated flow theory in terms of fundamental hydraulic properties such as diffusivity, conductivity and potential [6-9]. The $\sqrt{t}$ relationship can be derived by applying Richard's equation to one-dimensional unsaturated flow in a semi-infinite medium. It has also been shown to be valid for many other porous materials in addition to cement-based materials.

However, a number of researchers have reported results contrary to the expected linear $\sqrt{t}$ relationship, and there is much debate about the factors causing such anomalous behaviour [9-15]. For example, Hall et al. [10] showed that water uptake in cement-based materials is unusually low when compared to organic fluids; this was attributed to hydration of unreacted cement and swelling of hydrates on wetting. The chemo-mechanical changes restrict pore throats and reduce pore connectivity, reducing long-term water absorption. Taylor et al. [11] provided further evidence in support of this. Lockington and Parlange [12] defined a generalised sorptivity considering that moisture diffusivity varies with time in response to changes in the pore structure caused by these chemo-mechanical interactions. The anomaly may also be attributed to gravitational effects that retard capillary rise, particularly in samples containing large pores [13, 14]. Other factors such as non-homogeneous microstructure and gradients in initial water content have also been suggested [15], but not yet rigorously tested [16].

* Corresponding author. Tel: +44 20 7594 5956, E-mail: hong.wong@imperial.ac.uk

Since capillary absorption testing is carried out on pre-dried samples, often at elevated temperatures to accelerate drying, it is plausible that the presence of microcracks can be a factor causing anomalous water transport. The practical significance of this is the fact that most concrete structures experience drying and so are expected to be microcracked. It has long been suspected that microcracks facilitate ingress of aggressive agents that would impact durability. Yet, very few studies have directly characterised the microcracks and correlated their characteristics to mass transport properties and in particular capillary absorption [17-19]. The lack of studies is partly due to experimental difficulties in making direct measurements of microcracks that are small, scattered and non-uniformly distributed. This is in contrast to the considerable research on water transport in concrete containing mechanically-induced damage, where the cracks are larger (visible to naked eye), well-controlled and propagate through the sample. A number of studies have also attempted to simulate capillary absorption in concrete (e.g. [20, 21]), but none have taken into account the effect of microcracks. This is largely due to the complexity (length scales) involved when simulating a representative volume of concrete at sufficiently high resolution to capture the effects of microcracks [22].

This study aims to enhance the understanding of how drying-induced microcracking influences water absorption by capillary suction. A range of pastes, mortars and concretes were prepared and dried to equilibrium via several conditioning regimes to generate varying degrees of microcracking. The microcracks were quantified using fluorescence microscopy and related to water absorption characteristic in order to explain the observed anomalous behaviour.

2. Experimental

2.1 Materials and mix proportions

The cement used was CEM I 32.5 R with oxide composition of 63.4% CaO, 20.6% SiO_2, 5.6% Al_2O_3, 2.4% Fe_2O_3, 1.6% MgO, 0.2% Na_2O, 0.7% K_2O, 2.9% SO_3 and < 0.1% Cl. Its potential phase composition (Bogue) was estimated to be 52.7% C_3S, 19.3% C_2S, 10.6% C_3A, 7.4% C_4AF by mass. Loss on ignition, fineness and specific gravity of the CEM I were 2.1%, 290.5 m^2/kg and 3.06, respectively. Thames Valley sand (MSA= 2.5 & 5 mm) and crushed limestone (MSA= 10 & 20 mm) were used as fine and coarse aggregates respectively. Limestone was selected as coarse aggregate because of its high stiffness and low shrinkage. This increases the aggregate/paste property contrast, the amount of aggregate restraint and therefore the potential for microcracking. The limestone complied with BS EN 12620:2002+A1 overall grading while the sand complied with BS 882:1992 medium grading. Their particle size distributions are shown in Fig. 1. Table 1 provides their specific gravity, 24-hour water absorption, and moisture content. Batch water was adjusted to account for aggregate absorption so that the target free w/b ratio was achieved in the cement paste.

Mixes were designed according to the absolute volume method and their proportions are shown in Table 2. These include two concretes (C10 & C20), two mortars (M2.5 & M5) and three pastes (P-OPC, P-GGBS & P-PFA). The water/binder (w/b) ratio ranged from 0.35 to 0.50. Concrete and mortar mixes were prepared at the same free w/b ratio (0.50) and total aggregate volume fraction (60%), but with maximum size of aggregate (MSA) of either 2.5, 5, 10 or 20 mm. Aggregate size was varied because it influences the amount of drying-induced shrinkage stress and microcracking, as shown in earlier theoretical and experimental work (e.g. [23-28]. Total aggregate content was set at 60% vol. so that the paste fraction and hence total porosity were the same to allow meaningful comparison. A value of 60% vol. aggregate was chosen because of the difficulty with compacting mortars with sand content higher than this. Incomplete compaction produces excess air voids that would be another variable influencing mass transport [29]. P-GGBS and P-PFA are pastes with 75% CEM I replaced with GGBS and PFA. These mixes came from an earlier study [30] and they represent two common grouts used for encapsulating low/intermediate level radioactive wastes [31].

2.2 Samples

Ninety-three disc samples of 100 mm diameter (∅) and thickness (t) of 20 mm, 25 mm or 50 mm were prepared. Sample thickness was chosen to represent the typical size of cover to steel reinforcement in concrete structures. Thus by varying thickness and maximum aggregate size, samples with t/MSA ratio ranging from 2.5 to 20 were obtained (Table 3). Three to five replicate discs were prepared and tested for each mix, conditioning regime and t/MSA ratio.

Concretes and mortars were batched in a pan mixer by dry mixing cement and aggregates for 30s, followed by water addition and wet mixing for a further 3 min. Pastes were batched in a Hobalt mixer. Samples were cast in steel moulds and compacted in two to three layers on a vibrating table until no significant release of air bubbles was observed. All samples were cast to the required thickness except for P-GGBS and P-PFA, which were cast in 200 mm tall cylinders.

The compacted samples were covered with plastic sheet and wet hessian at room temperature (21°C) for the first 24 hours. Afterwards, they were demoulded and sealed with at least 6 layers of cling film and placed in sealed plastic bags for curing at 21°C for 28 days. Periodic weighing of the sealed samples found no significant weight change. The cylinders for P-GGBS and P-PFA were cured in a humid environment (> 90% RH) for 5 years. These were then sectioned using a diamond abrasive cutter to produce 20 mm thick discs spanning the height of the cylinder.

2.3 Conditioning regimes

After curing, the discs were unwrapped and subjected to five conditioning regimes by drying to mass equilibrium. The conditioning regimes were: a) stepwise drying at 21 ± 1°C from 93% RH to 86%, 76%, 66% and 55% RH, b) drying at 55% RH, 21°C, c) 0% RH, 21°C, d) oven drying at 50°C, 7% RH, and e) oven drying at 105°C. The purpose of the conditioning regimes is to produce samples with varying degrees of microcracking and moisture contents. Furthermore, it is well known that moisture state has a huge influence on measured water absorption and so it is important to condition samples to a uniform state prior to testing to allow meaningful comparison between mixes. Table 3 lists all the samples prepared. For brevity, stepwise drying conditioning regime (93% RH → 55% RH) is shown as 55% R* (with an asterisk). The different sample types allow us to establish not only the effect of drying, but also any potential size effects on water absorption.

Prior to conditioning, the circumference of each disc was sealed with two layers of waterproof adhesive tape to induce unidirectional drying. This is deemed to be a more realistic representation of how most structures dry in service. The required conditioning RH at 21°C was obtained using appropriate saturated salt solutions [32], these were KNO_3 (93% RH), KCl (86% RH), NaCl (76% RH), $NaNO_3$ (66% RH), $Mg(NO_3)_2$ (55% RH) and $MgCl_2$ (33% RH). Silica gel was used to achieve 0% RH. For the stepwise regime (55% RH*), samples were dried to equilibrium at each RH step before moving to the next lower RH. For all other regimes, samples were dried directly at the required temperature and humidity. Drying was carried out in either an enclosed box in a temperature controlled lab (21± 1°C) or in an oven; both contained fans to circulate air and soda lime to avoid carbonation. The RH was monitored regularly and the salt solution or silica gel were replaced when necessary. Samples were weighed periodically and equilibrium was assumed when the mass loss was less than 0.01% per day. Fig. 2 shows an example of the change in sample moisture content with conditioning until equilibrium for two replicate samples from the same mix.

Samples dried at 50°C and 105°C were cooled to room temperature (21± 1°C) in a vacuum desiccator containing silica gel for 24 hours to prevent moisture from re-entering the samples during cooling, prior to capillary absorption testing. The mass before and after cooling was recorded and the difference was always less than 0.01%, implying constant moisture content. The time required for each conditioning regime to complete were around 14 days for 105°C, 2 months for 50°C, 7% RH and 10 months for stepwise drying at 21°C, 55% RH*. The moisture content of samples after conditioning at 21°C, 55% RH* ranged from 3.1% to 3.9%, while the 50°C, 7% RH dried samples had moisture content ranging from 0.8% to 1.3% relative to the 105°C dried mass. The corresponding degrees of saturation were ~40% and ~10% for conditioning at 21°C, 55% RH* and 50°C, 7% RH respectively.

2.4 Capillary absorption

Absorption was determined using conventional gravimetric measurement in a simple vertical capillary rise setup by monitoring the increase in sample mass over time at ambient temperature (21± 1°C). The flat surface of each disc was placed on two plastic rods in a tray containing shallow water to a depth of about 1-2 mm from the bottom of the disc (Fig. 3) to allow free access of water and to simulate unidirectional absorption. The amount of water uptake with time was then measured with an electronic balance accurate to 0.01 g until saturation. Weighing was carried out at frequent intervals: typically at 5, 10, 15, 20 and 30 minutes, then every 15 minutes for the next hour, and then approximately every hour for the next 6 hours. Subsequently, daily readings were taken until the sample reached saturation. At this stage, the capillary moisture content of the sample is close to the vacuum saturated porosity. The difference is typically less than 1-2% (absolute) mainly due to filling of entrapped air voids when vacuum saturated.

Prior to each weighing, excess surface water was removed with dampened cloth and weighing was completed quickly (within 30s) without stopping the clock. A loose fitting lid was used to cover the tray to produce a humid environment to avoid drying of the sample during testing. Care was taken to ensure that condensates did not form underneath the cover and drop on to the sample. Water level was maintained periodically. The measured cumulative absorption was plotted against square-root of elapsed time. For one-dimensional absorption into an unsaturated semi-infinite homogeneous medium, cumulative absorption is given by the following expression [6-8]:

$$i = S_o\sqrt{t} + a \qquad \textbf{Eq. 1}$$

Where i is the cumulative absorbed water per unit area of the inflow face (g/m^2), S_o is the sorptivity coefficient ($g/m^2.min^{0.5}$) and a is a small fitting constant arising from minor surface effects mainly due to the filing of pores on the sample surface. The sorptivity coefficient S_o was determined from the slope of the best-fit line drawn across at least ten readings taken from the start of the test. This was repeated for three to five replicate discs for each mix and conditioning regime. Finally, the accessible porosity was estimated by measuring the volume of water absorbed from the preconditioned state to a vacuum saturated-surface dry condition, and divided by sample volume.

2.5 Imaging drying-induced microcracks

Fluorescence imaging was carried out to study drying-induced microcracks. The surface exposed to drying and cross-section were imaged to characterise surface and internal microcracking. After conditioning, replicate disc samples were pressure-impregnated from the flat top surface with a low viscosity fluorescent-dyed epoxy using compressed air at 0.7 MPa for 6 hours. They were then left to cure for 2 days at room temperature to allow epoxy to harden. Following that, the discs were ground to remove excess epoxy and to expose surface microcracks impregnated with fluorescein resin. Subsequently, the disc was illuminated with a 15 W UV lamp in a dark room to induce fluorescence and imaged with a 24 MP digital SLR camera. The camera was operated at low ISO, small aperture to increase depth of field and slow shutter speed to achieve adequate exposure. This gave a macro view of surface microcracking.

An 8 mm thick slice was extracted through the centre of the impregnated disc by sectioning with a diamond abrasive cutter. The slice was then ground using silicon carbide paper 80 and 120 grit size to obtain a flat surface for high resolution imaging. A large number of overlapping images were captured at 50× magnification (2048 ×1536 pixels, pixel size 0.89 µm) using a petrographic microscope (Olympus BX51) in fluorescence mode. The images were then aligned and stitched to produce a high-resolution montage of the cross-section. The microcrack width, length and density were measured on three replicate cross-sections using image analysis. Crack density was defined as the total length of microcracks divided by image area. Full details of the analysis are given in [19, 33].

2.6 Imaging water absorption

To study the movement of water penetration front during capillary absorption, the sorptivity test (Fig. 3) was repeated on a cross-section of replicate samples using water dyed with 1% wt. fluorescein ($C_{20}H_{12}O_5$), which acts as a tracer. The test was carried out in a dark room, with the sample illuminated with a pair of 15W UV lamps to induce fluorescence and imaged with a 24 MP digital single-lens reflex (SLR) camera. A schematic of the imaging setup is shown in Fig. 4. The camera was operated at a small aperture to increase the depth of field and at slow shutter speed to obtain adequate exposure. This setup mimics the sorptivity test and allows continuous imaging without disturbing the sample and water absorption process.

An example of the obtained fluorescence image taken after two hours of capillary absorption is shown in Fig. 5b. This is compared with an image from a replicate sample (Fig. 5a) treated in the same way, but captured with normal lightning with tap water (no fluorescein dye). It can be seen that both images show similar water penetration depths and characteristics. The sample edges seem to show slightly shallower penetration depths compared to internal regions. This could be due to microstructural heterogeneities at the cast surface. Nevertheless, the addition of dye and the use of fluorescence imaging greatly enhances the visibility of the wetted region and absorbed water front compared to imaging under normal light.

The samples were imaged at approximately 1-minute intervals for the first 10 minutes, then at 10-minute intervals for the next hour, 30-minute intervals for the next 6 hours and at 24-hour intervals until full saturation. Subsequently, image analysis was performed using ImageJ to measure the area of the wetted region and penetration depth. The boundary of the penetration front was carefully traced on the enlarged image and then segmented to produce a binary image of the wetted region, from which area measurement was carried out. This was repeated for various exposure periods and the results compared with gravimetric data.

3. Results

3.1 Cumulative absorption vs. $t^{1/2}$ plots

Fig. 6 and Fig. 7 show examples of cumulative absorption (mass per unit inflow area) against square-root of elapsed time ($\sqrt{t}$) for concrete, mortar and paste with different maximum size of aggregate, sample thickness and conditioning regime. Note that the plots show data from the first 3 days of measurement, longer-term data were truncated for clarity. Replicate samples produced very similar water absorption characteristics; hence these are not shown for clarity. The Y-axes are plotted on slightly different scales, again to improve the clarity of the presentation.

The slopes of the absorption plot, i.e. the sorptivity coefficient S_o as calculated with Eq. 1, are shown in Table 4 and Table 5. Each result is an average of three replicates and precision is expressed as standard error (= $\sigma/n^{½}$). Measured sorptivity S_o ranged from 18 to 240 g/m^2.min$^{0.5}$. The accessible porosity ranged from 9 to 28%. Increasing drying severity or w/b ratio increases sorptivity, total absorption at saturation and accessible porosity. Time to full saturation was slightly accelerated. However, changing the maximum size of aggregate or sample thickness (at constant aggregate content) did not produce a significant effect compared to drying. Thinner samples achieved saturation in a shorter time.

These observations are expected because water absorption is dependent on the amount of capillary porosity and degree of water saturation. Samples with low saturation degree have more empty pores and so are able to provide higher capillary suction to drive absorption [34, 35]. Therefore, a greater amount and rate of absorption occurred in oven-dried

samples compared to those gently dried at room temperature. However, there is little difference between the absorption profiles of 50°C compared to 105°C dried samples. This is because most of the capillary pores has emptied at 50°C and further drying to 105°C only caused a slight reduction in mass (0.8% to 1.3%), probably from the evaporation of gel water or decomposition of ettringite.

3.2 Anomalous absorption

On closer inspection of the absorption plots, it can be seen that some samples displayed a departure from linearity between cumulative absorption and square-root of time. The absorption plots of these samples appear to show a sigmoidal / *S*-shaped trend with an inflection point, instead of the expected linear relationship. Moreover, the extent of the anomalous behaviour increases in samples that were subjected to more severe drying (21°C/0% RH, 50°C/7% RH or 105°C) prior to testing. This behaviour is evident regardless of sample thickness and aggregate size.

A clear indication of this is seen in Fig. 7d. The P-GGBS paste dried at 0% RH showed an initial mass gain followed by a more rapid mass gain before achieving saturation. This is similar to a logistic growth function whereby the variable increases exponentially. After some time, the growth rate decreases and the function levels off, forming an s-shaped curve. The non-linearity is also similar to that reported by Griffin et al. [36] who studied water absorption in pressed fired clay bricks that consist of an exterior skin with low sorptivity and interior material with high sorptivity. The time at which the inflection occurred, coincided with the appearance of triple-branching map cracking patterns on the top surface of some samples. The significance of this will be discussed later. In contrast, the gently dried (at 55% RH) pastes showed a linear mass increase followed by a cross-over to a slower rate of mass gain as the samples reach saturation.

The coefficient of determination (R^2) from least squares linear regression to obtain S_o for all samples ranged from 0.909 to 1.000 (Tables 4 & 5). The R^2 values for severely dried samples were consistently lower than those of the gently dried samples, in line with the observed anomalous absorption in the former. To examine this further, the absorption data for each sample were divided into two stages and linear regression was applied to obtain a "sorptivity" coefficient for each stage. This is schematically shown in Fig. 8b. The best-fit line for the first stage was drawn across the data before inflection (typically within the first hour) and the best-fit line for the second stage drawn across subsequent data up to the first 7 hours of measurement or until saturation. The slope *S1* and *S2* denote the sorptivity measured in each stage respectively (Tables 4 & 5). It is observed that the new coefficients of determination (R^2) for *S1* and *S2* are greater than 0.99 for all samples regardless of drying regime, MSA and sample thickness, suggesting an improved fit.

Fig. 9 shows scatter plots for *S1* and *S2*/*S1* ratio plotted against S_o for all samples. Obviously, one should expect S_o = *S1* = *S2* for a perfect linear behaviour, but this is not the case. The data show that *S1* is smaller than S_o, while *S2* is larger than *S1* in all but a handful of samples. The difference between S_o, *S1* and *S2* increases with drying severity. *S2*/*S1* ratios range from 0.9 to 3, increasing with drying severity as seen in Fig. 9 and Fig. 10. The trend is again consistent regardless of sample thickness and aggregate size. The *S2*/*S1* ratios for 50 mm thick samples are marginally higher than the 25 mm thick samples.

3.3 Effect of sample thickness and maximum aggregate size

Fig. 11 plots the sorptivity coefficients against *t*/*MSA* ratio to examine the influence of sample thickness (*t*) and maximum aggregate size (*MSA*). To produce these plots, samples of the same thickness and conditioning regime were grouped, and the sorptivity coefficients normalised to the average of each group. Although there is a slight scatter in the data, Fig. 11 shows that the S_o, *S1* and *S2* coefficients are relatively constant for the entire range of the *t*/*MSA* ratio investigated. The overall trend suggests that the sorptivity coefficients are relatively independent of *t/MSA* compared to other factors such as mix proportions, curing age and conditioning regime. Therefore, water absorption does not display significant size effects which is consistent with an earlier study [19].

3.4 Drying-induced microcracks

Fig. 12 presents fluorescence images of sample surfaces and cross-sections. All samples displayed some amount of microcracking even those that were gently dried at 21°C. Those exposed to severe drying show surface map-cracking that is a typical characteristic of shrinkage-induced microcracking [24, 27, 28, 37-39]. On the cross-section, the microcracks propagate approximately perpendicularly to the exposed surface to depths of several mm, but show little tendency for branching (Fig. 12d). Locations with deep epoxy impregnation coincide with the presence of microcracks, which are detectable at higher magnification. The microcracks occur through cement paste or along the aggregate-paste interface, propagating from one particle to a neighbouring particle where they either arrest or travel around the aggregate particle. The microcracks rarely propagate through aggregate.

Fig. 13 shows the average width, total length and density of internal microcracking for selected 50 mm thick samples with different conditioning regime and *t/MSA* ratio. Consistent with earlier studies [19, 40], the observed microcrack widths ranged between 1 and 60 µm, with over 80% of the microcracks having widths less than 10 µm and lengths shorter than 100 µm. As expected, the crack width, length and density increased in samples subjected to a more severe

drying regime. Samples that were dried at 21°C also showed microcracking, but significantly less extensive compared to samples dried at elevated temperature.

Sample P-GGBS showed a somewhat different crack morphology. In addition to the micron sized map-cracking described above, it also contained cracks of up to 100 μm in width that formed at early ages due to restrained shrinkage and partially healed via subsequent hydration. These cracks traverse through the thickness of the disc and details are given in an earlier study [30]. The severe microcracking seen in P-GGBS is probably compounded by the high autogenous shrinkage in slag cements and the high self-desiccation tendency in a low w/b ratio mix.

It should be noted that the observed microcracks are unlikely to have been caused by sample preparation, for example damage from cutting, grinding or polishing because most samples were cast to the required thickness and were epoxy impregnated prior to any of these procedures. The epoxy fills in cracks and voids, hardens and preserves these structures. Furthermore, impregnation was not carried out under vacuum to avoid the possibility of additional drying induced cracking. If any new microcracks form during sample preparation, these would not be epoxy-filled and therefore not imaged with fluorescence microscopy. Thus, the detected microcracks must either be inherent or induced by the imposed drying regime, and they are interconnected to the exposed surface.

3.5 Imaging water absorption

Fig. 14 presents examples of fluorescence images of the same sample captured during water absorption at different times from initial contact up to saturation following the procedure described in Section 2.6. The sample is a 0.5 w/c ratio, 28-day cured, 50 mm thick paste conditioned at 50°C/7% RH to equilibrium prior to absorption. The images clearly show that the initial water uptake is dominated by absorption into the microcracks, producing a highly uneven water penetration front. The microcracks are approximately perpendicular to the surface and extend up to several mm into the sample, in agreement with image analysis presented in the preceding section.

The microcracks fill up and become saturated with water very quickly. Subsequent uptake occurs through the uncracked regions drawing water from the wetted surface as well as from microcracks acting as reservoirs. The penetration front spreads in all directions from the microcracks until it meets and merges with the penetration front from adjacent cracks. It is worth noting such behaviour has been observed for larger (macro) cracks using neutron radiography e.g. [41, 42], but none of these studies have looked at its effect on the $i \propto \sqrt{t}$ relationship. The initially uneven front smooths out over time and subsequently advances approximately parallel to the exposed surface. A slight delay occurs near the vertical sides, suggesting a denser microstructure in these regions. No further microcracks are encountered as the penetration front moves through the sample. The sample becomes saturated after ~1 day of absorption.

Fig. 15 presents another set of time series fluorescence images of a replicate sample, but subjected to mild step-wise drying at 21°C, 55% RH prior to water absorption. The wetting front is irregular at very early stages of absorption, but this is substantially less significant compared to Fig. 14. The water uptake is less affected by drying-induced microcracking and the wetting front advances in a more even manner compared to severely dried samples. Again, a slight delay is observed near the sides, suggesting a denser microstructure in these regions.

Image analysis was carried out to measure the water penetration depth. The penetration front was traced, then the wetted area segmented, measured and plotted against $\sqrt{t}$. Results are shown in Fig. 16. It can be seen that the cumulative area has a sigmoidal relationship with $\sqrt{t}$ and bears remarkable resemblance to the cumulative absorption plot obtained gravimetrically on replicates. The anomalous behaviour is greater in samples subjected to more severe drying. Furthermore, the times to the first inflection point and to full saturation obtained from image analysis are similar to those from gravimetric measurements. This shows that the wetted region seen on the fluorescence images is a good representation of actual water penetration, despite the fact that the wetted area and total absorption are not exactly equivalent due to non-homogeneous distribution of water content (caused by surface drying, heterogeneity in microstructure or other factors).

4. Discussion

4.1 Possible causes of anomalous absorption

A number of conditions must be satisfied in order for cumulative absorption to scale linearly to $\sqrt{t}$ in a single-sided water absorption test [8] and these should be examined in relation to the current study. The conditions are: i) sample has constant cross-section; ii) water is freely available at the wetting face; iii) flow is strictly one-dimensional; iv) initial water content of the sample is uniform; v) gravitational effects are negligible; vi) sample is homogenous; and vii) sample does not undergo microstructural changes during testing. The first four conditions are usually well-controlled in laboratory experiments such as in this study and therefore should not be of concern. However, achieving a uniform moisture content prior to absorption can be difficult for cement-based materials particularly when gently dried at ambient temperature. In this study, sample conditioning was carried out over a period of 10 months until equilibrium

(mass loss < 0.01% per day, Fig. 2) and this should suffice. In any case, the gently dried samples showed the least anomaly in absorption behaviour.

Gravitational effects may retard vertical capillary rise in samples with large pores that exert weak capillary forces. For example, departures from linearity have been observed in poorly compacted concretes [13] and autoclaved aerated concretes [14]. To ascertain the significance of this effect in the present study, we estimate the capillary rise height in microcracks and compare this to sample thickness. At static equilibrium, the height of capillary rise is obtained by balancing capillary and gravitational forces [43]. The capillary pressure p_c according to the Young-Laplace equation is $p_c = 2\gamma \cos\theta \,/r$, where γ is the surface tension (0.0728 N/m at 20°C), θ is the liquid/solid contact angle (°) and r is the radius of capillary (m). At static equilibrium, capillary pressure is equal to hydrostatic pressure $p_h = \rho g h \sin\phi$, where ρ is the fluid density (kg/m^3), g is the gravitational constant, h is the capillary rise height (m) and ϕ is the inclination angle of microcracks to the inflow surface (°). Hence, the equilibrium capillary rise height h_{eq} (m) can be expressed as:

$$h_{eq} = \frac{p_c}{\rho g \sin\phi} = \frac{2\gamma \cos\theta}{\rho g r \sin\phi} \qquad \textbf{Eq. 2}$$

For simplicity, we assume $\theta = 0°$ (fully wetting) and $\phi = 90°$ since drying-induced microcracks are approximately perpendicular to the inflow surface (Figs. 12d and 14a). The microcrack width is typically less than 10 µm (Fig. 13a), hence the equilibrium capillary rise height h_{eq} must be at least 2.97 m. This is much larger than the microcrack total length (Fig. 13b) or the sample thickness (20-50 mm). Therefore, gravitational effects can be considered negligible due to the strong capillary forces exerted by microcracks and the relatively short distances over which water absorption occurs.

The sixth condition is sample homogeneity. Layered or non-uniform samples could deviate from the ideal $i \propto \sqrt{t}$ behaviour because of variations in transport properties with depth. For example, samples that have experienced excessive segregation, bleeding or carbonation could, in theory, produce the sigmoidal behaviour seen in this study if the denser part of the sample (high aggregate content, low w/b ratio) is exposed to wetting. Absorption would be initially delayed and then accelerated as the water front travels through the more porous region. However, this explanation does not fit our observations because the anomalous behaviour was dependent on drying regime rather than mix composition. Furthermore, all samples were well-compacted, but showed little indication of bleeding during preparation or aggregate segregation in the cross-section. There was no significant difference in air content between samples so this could not be a factor influencing measured transport [29]. The samples have a wide range of *t*/MSA ratio from 2.5 to 20, are sufficiently large to be representative of the bulk and displayed no size effects (Fig. 11).

The last condition (vii) requires careful scrutiny because it is well known that drying and wetting induces microstructural changes in cement-based materials, therefore this criterion is unlikely to be met. Indeed, some studies have attributed anomalous absorption to swelling of hydrates and further hydration of unreacted cementitious materials on rewetting [10-12]. In addition, dissolution and leaching of soluble compounds such as portlandite coarsens the microstructure, but may cause pore blockage if the dissolved species are transported and deposited near the surface. Studies comparing the absorption of various fluids in cement-based materials have shown that organic liquids obey the $i \propto \sqrt{t}$ behaviour well, but water is markedly deviant [10, 16, 44, 45].

However, these effects do not explain the anomaly observed in this study. Swelling of hydrates or further hydration would cause the cumulative absorption to be lower and increasingly deviate from the expected $i \propto \sqrt{t}$ behaviour, which does not correspond to our observations. The anomalous behaviour was seen in relatively young and well hydrated (5-year old) samples, and the anomaly occurred at very early stages of absorption (within the first hour) so the effect of further hydration and swelling should be small. Furthermore, the gently dried samples did not show deviation from the linear $\sqrt{t}$ behaviour. The samples were sealed cured and would have self-desiccated to some extent prior to external drying. Therefore, leaching and movement of dissolved species to the surface causing pore blockage is unlikely to be significant.

4.2 Proposed mechanism

Our results collectively show that the anomalous absorption seen here is related to microcracking and that the extent of the anomaly increases with drying severity. The proposed mechanism is as follows. Drying increases the amount of accessible porosity and coarsens the capillary pore structure leading to a more open microstructure [46, 47]. Furthermore, volumetric shrinkage of the cement paste induces tensile stresses when restrained by either rigid aggregate particles or the internal material that dries at a slower rate than the surface. This induces surface microcracking when the tensile strength is exceeded. Samples dried at elevated temperatures experience more microcracking due to the steeper thermal and moisture gradients. These factors explain the characteristics of the observed microcracks, which are consistent with other studies [24, 28, 37-39].

When the sample is exposed to water, initial uptake (S1) is dominated by absorption into the microcracks because they provide a continuous flow path that is much less tortuous compared to capillary pores (Fig. 14). When the microcracks

become water filled, subsequent uptake (S2) occurs via capillary pores from the wetted sample surface as well as from the saturated microcracks causing the water front to spread vertically and laterally. The saturated microcracks effectively act as water reservoirs that increase the surface area of the sample accessible to water and this increases absorption. However, these effects are not accounted for in the absorption plot because cumulative absorption *i* (Eq. 1) is calculated assuming constant inflow surface area, i.e. the sample cross-sectional area. Therefore, the calculation under-estimates S1 while S2 is over-estimated.

Therefore, the microcracks appear to accelerate subsequent absorption, which seems counterintuitive. The effect described above produces an apparent transition that deviates from $\sqrt{t}$ kinetics to a more rapid sorption rate (S1 to S2, Fig. 8b). This is marked by an inflection point in the *i* vs. $\sqrt{t}$ plot. The position of the inflection relates to the depth of microcracking, and is delayed in samples with extensive and deeper microcracks (e.g. P-GGBS, Fig. 7d). If the microcracks traverse through the sample thickness, then the time of the inflection coincides with appearance of map cracking pattern on the top (dry) surface (e.g. Fig. 8a). Subsequent absorption occurs through the non-cracked material until the wetting front reaches the top surface. Finally, absorption rate decreases as the sample saturates. The mechanism described above is consistent with the observation that all sorptivity coefficients (S_o, S1, S2) increased with increase in drying severity (Tables 4 & 5). It also explains the increase in S2/S1 ratio with drying (Figs. 9 & 10).

4.3 Implications

Although the drying conditions imposed in our study are more severe than natural drying in real structures, they are similar to those employed in many studies and recommendations in codes of practice. Sorptivity is a commonly measured transport property and often used as a performance indicator. Therefore, the effect of microcracks has important implications that need to be considered when collecting, analysing and comparing results. In particular, the non-linear behaviour creates uncertainties regarding the way in which sorptivity should be defined and calculated. Since the anomaly occurs at very early stages of absorption (within the first few hours), this effect can easily be overlooked if a small number of measurements are taken during testing. For example, NT Build 368 and BS EN 13057 recommend only 5-6 measurements during the first 6 hours. Some standards allow calculation of sorptivity from just 2 measurements (initial, final) [2, 3] and such sparse data collection is adopted in many studies. Sorptivity may not be a meaningful parameter if it is calculated in the conventional manner. For example, if the coefficient of determination R^2 is less than 0.99, then the data needs to be examined carefully for systematic curvature. Gentle drying reduces microcracking and the absorption anomaly, but such a conditioning regime is impractical because of the very long time required to condition representatively thick samples.

Most concrete structures are exposed to drying and wetting environments. Therefore, real structures contain microcracks and water absorption via capillary suction is an important transport process influencing durability. The fact that surface microcracking accelerates water absorption is a concern because this increases the rate and amount of dissolved aggressive species penetrating the concrete cover, thus accelerating degradation (e.g. reinforcement corrosion). However, real structures generally experience less extreme moisture/temperature variations over shorter time intervals and less complete drying compared to that imposed in this study. The samples tested here are likely to be more microcracked, and the observed effects represent a worst-case scenario in relation to most practical situations. Microcracks can self-heal in a wet environment, thus subsequent transport rates through microcracks will decrease, but there is the possibility of cracks opening/widening due to cyclic wetting/drying or structural loading. Clearly, further work is needed to study the extent of microcracking in structures in service and to better understand its influence on long-term durability.

5. Conclusions

The aim of this study is to enhance the understanding of how drying induced microcracking influences water absorption via capillary suction. Over 90 paste, mortar and concrete samples of a range of binder type, w/b ratio, aggregate size, t/MSA ratio and curing age were prepared. Samples were conditioned to equilibrium by gentle stepwise drying at 21°C from 93% to 55% RH, or by drying at 21°C / 55% RH, 21°C / 0% RH, 50°C or 105°C to generate varying amounts of microcracking prior to testing. The main findings are:

a) The measured sorptivity S_o for all samples ranged from 18 to 240 g/m^2.min$^{0.5}$, and accessible porosity ranged from 9 to 28%. Sorptivity, total absorption and accessible porosity increase with an increase in w/b ratio or drying severity. However, maximum size of aggregate, sample thickness and *t*/MSA ratio did not produce a significant effect.

b) Drying induces surface map cracking with widths < 100 μm that propagate approximately perpendicular into the sample to depths of several mm. The width, length, density and depth of microcracks increase with increase in drying severity.

c) Gently dried samples display a strong linear relationship between cumulative absorption *i* and square-root of time *t*, with a coefficient of determination R^2 consistently greater than 0.99. However, severely dried samples deviate

from the expected $i \propto \sqrt{t}$ relationship, the degree of non-linearity increasing with an increase in drying and microcracking.

d) Presence of microcracks changes the *i* vs. $\sqrt{t}$ relationship to sigmoidal / *S*-shaped. This can be approximated as: an initial absorption stage that is linear to $\sqrt{t}$ with slope *S1,* followed by a transitional stage (inflection) that deviates from $\sqrt{t}$ kinetics, and a later stage where *i* is again linear to $\sqrt{t}$ with slope *S2* until the sample saturates. The ratio *S2*/*S1* increases with drying severity and microcracking.

e) Fluorescence imaging shows that the initial stage (*S1*) is dominated by absorption into surface microcracks causing a highly irregular penetration front. Once the microcracks saturate, they effectively act as reservoirs, increasing the surface area accessible to water and accelerating subsequent absorption (S2). This produces the transition (inflection) point in the *i* vs. $\sqrt{t}$ plot. The penetration front spreads in all directions and merges with those from adjacent cracks, smooths out over time and advances ~ parallel to the exposed surface until saturation. These effects are not considered in the conventional sorptivity calculation since it assumes a constant inflow surface area, i.e. sample cross-sectional area.

f) Image analysis of cumulative water penetration reproduces the sigmoidal / *S*-shape relationship with $\sqrt{t}$ that is consistent with the cumulative absorption plot from gravimetric measurements. The position of the inflection point relates to the amount of microcracks, and is delayed in samples with extensive and deeper microcracks.

g) Sorptivity is an important transport property, but the anomalous behaviour creates uncertainties in the way in which it is defined, calculated or applied. This effect can be easily overlooked if a small number of measurements are taken during testing.

Acknowledgments

We would like to acknowledge the funding from the UK-China Scholarships for Excellence programme, provided by the UK Department for Business Innovation & Skills and the China Scholarship Council. We also thank Mr. Andrew Morris for his help with the laboratory work.

References

[1] BS EN 13057:2002 Products and systems for the protection and repair of concrete structures. Test methods. Determination of resistance of capillary absorption, British Standards Institution, 2002.

[2] BS EN 1015-18:2002, Methods of test for mortar for masonry. Determination of water absorption coefficient due to capillary action of hardened mortar, British Standards Institution, 2002.

[3] BS EN ISO 15148:2002+A1:2016 Hygrothermal performance of building materials and products. Determination of water absorption coefficient by partial immersion, British Standards Institution, 2016.

[4] NT BUILD 368 Concrete, repair materials: Capillary absorption Nordtest, 1991.

[5] ASTM C1585-13 Standard Test Method for Measurement of Rate of Absorption of Water by Hydraulic-Cement Concretes, ASTM International, 2013.

[6] C. Hall, Water movement in porous building materials—I. Unsaturated flow theory and its applications, Building and Environment, 12 (1977) 117-125.

[7] C. Hall, Water sorptivity of mortars and concretes: a review, Magazine of Concrete Research, 41 (1989) 51-61.

[8] C. Hall, W.D. Hoff, Water Transport in Brick, Stone and Concrete, 2nd ed., CRC Press2012.

[9] N.S. Martys, C.F. Ferraris, Capillary transport in mortars and concrete, Cement and Concrete Research, 27 (1997) 747-760.

[10] C. Hall, W.D. Hoff, S.C. Taylor, M.A. Wilson, B.-G. Yoon, H.W. Reinhardt, M. Sosoro, P. Meredith, A.M. Donald, Water anomaly in capillary liquid absorption by cement-based materials, Journal of Materials Science Letters, 14 (1995) 1178-1181.

[11] S.C. Taylor, W.D. Hoff, M.A. Wilson, K.M. Green, Anomalous water transport properties of Portland and blended cement-based materials, Journal of Materials Science Letters, 18 (1999) 1925-1927.

[12] D.A. Lockington, J.Y. Parlange, Anomalous water absorption in porous materials, Journal of Physics D: Applied Physics, 36 (2003) 760.

[13] C. Hall, M.H. Raymond Yau, Water movement in porous building materials—IX. The water absorption and sorptivity of concretes, Building and Environment, 22 (1987) 77-82.

[14] I. Ioannou, A. Hamilton, C. Hall, Capillary absorption of water and n-decane by autoclaved aerated concrete, Cement and Concrete Research, 38 (2008) 766-771.

[15] L.J. Parrott, Water absorption in cover concrete, Materials and Structures, 25 (1992) 284.

[16] C. Hall, Anomalous diffusion in unsaturated flow: Fact or fiction?, Cement and Concrete Research, 37 (2007) 378-385.

[17] Z. Yang, W.J. Weiss, J. Olek, Water Transport in Concrete Damaged by Tensile Loading and Freeze–Thaw Cycling, Journal of Materials in Civil Engineering, 18 (2006) 424-434.

[18] M. Şahmaran, V.C. Li, Influence of microcracking on water absorption and sorptivity of ECC, Materials and Structures, 42 (2009) 593-603.

[19] Z. Wu, H.S. Wong, N.R. Buenfeld, Influence of drying-induced microcracking and related size effects on mass transport properties of concrete, Cement and Concrete Research, 68 (2015) 35-48.

[20] L. Wang, T. Ueda, Mesoscale modeling of water penetration into concrete by capillary absorption, Ocean Engineering, 38 (2011) 519-528.

[21] S. Dehghanpoor Abyaneh, H.S. Wong, N.R. Buenfeld, Computational investigation of capillary absorption in concrete using a three-dimensional mesoscale approach, Computational Materials Science, 87 (2014) 54-64.

[22] S.D. Abyaneh, H.S. Wong, N.R. Buenfeld, Simulating the effect of microcracks on the diffusivity and permeability of concrete using a three-dimensional model, Computational Materials Science, 119 (2016) 130-143.

[23] T.T.C. Hsu, Mathematical Analysis of Shrinkage Stresses in a Model of Hardened Concrete, ACI Journal Proceedings, 60 371-390.

[24] J. Bisschop, J.G.M. van Mier, Effect of aggregates on drying shrinkage microcracking in cement-based composites, Materials and Structures, 35 (2002) 453-461.

[25] E. Schlangen, E.A.B. Koenders, K. van Breugel, Influence of internal dilation on the fracture behaviour of multi-phase materials, Engineering Fracture Mechanics, 74 (2007) 18-33.

[26] C. de Sa, F. Benboudjema, M. Thiery, J. Sicard, Analysis of microcracking induced by differential drying shrinkage, Cement and Concrete Composites, 30 (2008) 947-956.

[27] P. Grassl, H.S. Wong, N.R. Buenfeld, Influence of aggregate size and volume fraction on shrinkage induced micro-cracking of concrete and mortar, Cement and Concrete Research, 40 (2010) 85-93.

[28] A. Idiart, J. Bisschop, A. Caballero, P. Lura, A numerical and experimental study of aggregate-induced shrinkage cracking in cementitious composites, Cement and Concrete Research, 42 (2012) 272-281.

[29] H.S. Wong, A.M. Pappas, R.W. Zimmerman, N.R. Buenfeld, Effect of entrained air voids on the microstructure and mass transport properties of concrete, Cement and Concrete Research, 41 (2011) 1067-1077.

[30] H.S. Wong, N.R. Buenfeld, J. Hill, A.W. Harris, Mass transport properties of mature wasteform grouts, Advances in Cement Research, 19 (2007) 35-46.

[31] G.A. Fairhall, J.D. Palmer, The encapsulation of Magnox Swarf in cement in the United Kingdom, Cement and Concrete Research, 22 (1992) 293-298.

[32] F.E.M.O. Brien, The Control of Humidity by Saturated Salt Solutions, Journal of Scientific Instruments, 25 (1948) 73.

[33] Z. Wu, H.S. Wong, N.R. Buenfeld, Effect of confining pressure and microcracks on mass transport properties of concrete, Advances in Applied Ceramics, 113 (2014) 485-495.

[34] M. Nokken, R. Hooton, Dependence of Rate of Absorption on Degree of Saturation of Concrete, Cement, Concrete and Aggregates, 24 (2002) 20-24.

[35] J. Castro, D. Bentz, J. Weiss, Effect of sample conditioning on the water absorption of concrete, Cement and Concrete Composites, 33 (2011) 805-813.

[36] I.M. Griffin, C. Hall, A. Hamilton, Unusual water transport properties of some traditional Scottish shale bricks, Materials and Structures, 47 (2014) 1761-1771.

[37] C.L. Hwang, J.F. Young, Drying shrinkage of portland cement pastes I. Microcracking during drying, Cement and Concrete Research, 14 (1984) 585-594.

[38] K.O. Kjellsen, H.M. Jennings, Observations of microcracking in cement paste upon drying and rewetting by environmental scanning electron microscopy, Advanced Cement Based Materials, 3 (1996) 14-19.

[39] I. Maruyama, H. Sasano, Strain and crack distribution in concrete during drying, Materials and Structures, 47 (2014) 517-532.

[40] Z. Wu, H.S. Wong, N.R. Buenfeld, Transport properties of concrete after drying-wetting regimes to elucidate the effects of moisture content, hysteresis and microcracking, Cement and Concrete Research, 98 (2017) 136-154.

[41] M. Kanematsu, I. Maruyama, T. Noguchi, H. Iikura, N. Tsuchiya, Quantification of water penetration into concrete through cracks by neutron radiography, Nuclear Instruments and Methods in Physics Research Section A: Accelerators, Spectrometers, Detectors and Associated Equipment, 605 (2009) 154-158.

[42] P. Zhang, F.H. Wittmann, T. Zhao, E.H. Lehmann, Neutron imaging of water penetration into cracked steel reinforced concrete, Physica B: Condensed Matter, 405 (2010) 1866-1871.

[43] D. Gardner, A. Jefferson, A. Hoffman, Investigation of capillary flow in discrete cracks in cementitious materials, Cement and Concrete Research, 42 (2012) 972-981.

[44] M. Sosoro, Transport of organic fluids through concrete, Materials and Structures, 31 (1998) 162-169.

[45] M. Krus, K.K. Hansen, H.M. Künzel, Porosity and liquid absorption of cement paste, Materials and Structures, 30 (1997) 394-398.

[46] I. Maruyama, Y. Nishioka, G. Igarashi, K. Matsui, Microstructural and bulk property changes in hardened cement paste during the first drying process, Cement and Concrete Research, 58 (2014) 20-34.

[47] A.M. Gajewicz, E. Gartner, K. Kang, P.J. McDonald, V. Yermakou, A 1H NMR relaxometry investigation of gel-pore drying shrinkage in cement pastes, Cement and Concrete Research, 86 (2016) 12-19.

Table 1 Aggregate properties

Aggregate type	*MSA*: mm	Density: kg/m^3	Moisture absorption:%	Moisture content:%
Sand (2.5)	2.5	2437	0.38	0.21
Sand (5.0)	5	2540	0.52	0.21
Limestone (10)	10	2712	0.88	0.46
Limestone (20)	20	2750	0.84	0.40

Table 2 Mix proportions

Mix	CEM I: kg/m^3	PFA: kg/m^3	GGBS: kg/m^3	Water: kg/m^3	Free w/b	*MSA*: mm	Sand: kg/m^3	Limestone: kg/m^3	Aggregate vol fraction:%
C20	471.7	-	-	242.0	0.50	20	638.9	958	60
C10	471.7	-	-	241.8	0.50	10	633.7	951	60
M5	471.7	-	-	240.6	0.50	5	1524.0	-	60
M2.5	471.7	-	-	238.3	0.50	2.5	1462.2	-	60
P	1197.4	-	-	589.7	0.50	-	-	-	-
P-PFA	371.7	1115.1	-	624.5	0.42	-	-	-	-
P-GGBS	371.7	-	1115.1	520.4	0.35	-	-	-	-

Table 3 Conditioning regimes and t/MSA ratio

Series	Sample ID	*MSA*: mm	Thickness, *t*: mm	t/MSA	Conditioning regimes
I	C20:50	20	50	2.5	a) 105°C , b) 50°C/7% RH, c) 21°C/55% RH*
	C10:50	10	50	5	a) 105°C , b) 50°C/7% RH, c) 21°C/55% RH*
	C10:25	10	25	2.5	a) 105°C , b) 50°C/7% RH, c) 21°C/55% RH*
II	M5:50	5	50	10	a) 105°C , b) 50°C/7% RH, c) 21°C/55% RH*
	M5:25	5	25	5	a) 105°C , b) 50°C/7% RH, c) 21°C/55% RH*
	M2.5:50	2.5	50	20	a) 105°C , b) 50°C/7% RH, c) 21°C/55% RH*
	M2.5:25	2.5	25	10	a) 105°C , b) 50°C/7% RH, c) 21°C/55% RH*
III	P:50	-	50	-	a) 50°C/7% RH, b) 21°C/55% RH*
	P-PFA:20	-	20	-	a) 21°C/55% RH, b) 21°C/0% RH
	P-GGBS:20	-	20	-	a) 21°C/55% RH, b) 21°C/0% RH

** Stepwise drying by gradually decreasing RH from 93% to 86%, 76%, 66% and finally 55% at 21°C.*

Table 4 Average water sorptivity coefficients ± standard errors ($g/m^2.min^{0.5}$) of concretes and mortars. Values in brackets are the average coefficient of determination (R^2) from least squares linear regression.

Sample	t/ MSA	105°C			50°C			21°C/55% RH*		
		S_o	S1	S2	S_o	S1	S2	S_o	S1	S2
C20:50	2.5	190.5 ± 10.2 (0.989 ± 0.001)	91.7 ± 8.1 (0.996 ± 0.002)	210.5 ± 15 (0.998 ± 0.001)	170.1 ± 2.9 (0.996 ± 0.001)	138.1 ± 2.4 (0.999 ± 0.000)	184.8 ± 4.3 (0.999 ± 0.000)	91.9 ± 9.2 (0.999 ± 0.000)	85.5 ± 11.3 (0.999 ± 0.000)	92.9 ± 8.2 (1.000 ± 0.000)
C10:50	5	167.9 ± 14 (0.989 ± 0.001)	90.4 ± 0.2 (0.995 ± 0.005)	183.0 ± 1.5 (0.996 ± 0.001)	170.8 ± 0.8 (0.989 ± 0.002)	112.5 ± 7.4 (0.998 ± 0.002)	190.7 ± 13.2 (0.996 ± 0.001)	96.7 ± 12.2 (0.995 ± 0.001)	70.1 ± 6.9 (0.996 ± 0.001)	103.2 ± 13.5 (1.000 ± 0.000)
C10:25	2.5	172.5 ± 10 (0.993 ± 0.002)	115.4 ± 6.8 (0.999 ± 0.001)	183.9 ± 12.1 (0.997 ± 0.001)	140.5 ± 3.7 (0.995 ± 0.001)	107.5 ± 1.8 (0.997 ± 0.002)	153.8 ± 4.1 (0.999 ± 0.001)	80.0 ± 7.5 (0.995 ± 0.001)	64.2 ± 6.0 (0.996 ± 0.002)	83.8 ± 7.7 (1.000 ± 0.000)
M5:50	10	184.3 ± 4.0 (0.989 ± 0.001)	100.3 ± 2.4 (0.993 ± 0.001)	205.4 ± 6.5 (0.999 ± 0.000)	188.5 ± 13.6 (0.995 ± 0.001)	156.6 ± 7.3 (0.995 ± 0.002)	190.7 ± 15.4 (0.999 ± 0.002)	83.0 ± 3.8 (0.999 ± 0.000)	71.5 ± 7.1 (0.994 ± 0.001)	83.8 ± 3.8 (1.000 ± 0.000)
M5:25	5	195.8 ± 25.1 (0.989 ± 0.001)	113.2 ± 16.4 (0.997 ± 0.001)	213.5 ± 28.1 (0.997 ± 0.001)	187.6 ± 6.9 (0.996 ± 0.002)	174.9 ± 9.7 (0.997 ± 0.001)	178.0 ± 8.3 (0.994 ± 0.003)	81.7 ± 6.3 (0.999 ± 0.000)	71.4 ± 3.0 (0.994 ± 0.003)	82.7 ± 6.7 (0.999 ± 0.000)
M2.5:50	20	162.3 ± 4.6 (0.986 ± 0.002)	74.1 ± 6.9 (0.992 ± 0.001)	178.8 ± 5.4 (0.997 ± 0.001)	239.5 ± 1.2 (0.998 ± 0.001)	181.0 ± 15.5 (0.994 ± 0.003)	246.7 ± 1.1 (1.000 ± 0.000)	88.3 ± 3.5 (0.999 ± 0.000)	73.1 ± 2.7 (0.999 ± 0.000)	90.2 ± 3.5 (1.000 ± 0.000)
M2.5:25	10	197.2 ± 24.4 (0.985 ± 0.002)	102.2 ± 25.9 (0.994 ± 0.004)	218.4 ± 27.5 (0.997 ± 0.001)	205.8 ± 12.4 (0.999 ± 0.001)	195.9 ± 13.8 (0.999 ± 0.001)	196.5 ± 9.6 (0.997 ± 0.001)	93.5 ± 1.3 (0.999 ± 0.000)	89.9 ± 14.6 (0.998 ± 0.001)	91.5 ± 9.1 (0.999 ± 0.000)

Table 5 Average water sorptivity coefficients ± standard errors ($g/m^2.min^{0.5}$) of pastes. Values in brackets are the average coefficient of determination (R^2) from least squares linear regression.

Sample	t/MSA	21°C, 0% RH			21°C, 55% RH		
		S_o	S1	S2	S_o	S1	S2
P-PFA:20	-	221.1 ± 16.8 (0.999 ± 0.001)	182.8 ± 10.8 (0.999 ± 0.000)	229.9 ± 20.1 (0.999 ± 0.000)	127.4 ± 16.7 (1.000 ± 0.000)	125.0 ± 13.9 (1.000 ± 0.000)	132.1 ± 18.8 (1.000 ± 0.000)
P-GGBS:20	-	107.7 ± 20.3 (0.909 ± 0.031)	49.6 ± 12.2 (0.993 ± 0.001)	175.0 ± 13.9 (0.998 ± 0.003)	17.9 ± 3.8 (0.968 ± 0.009)	12.3 ± 2.3 (0.999 ± 0.001)	26.2 ± 5.2 (0.999 ± 0.001)

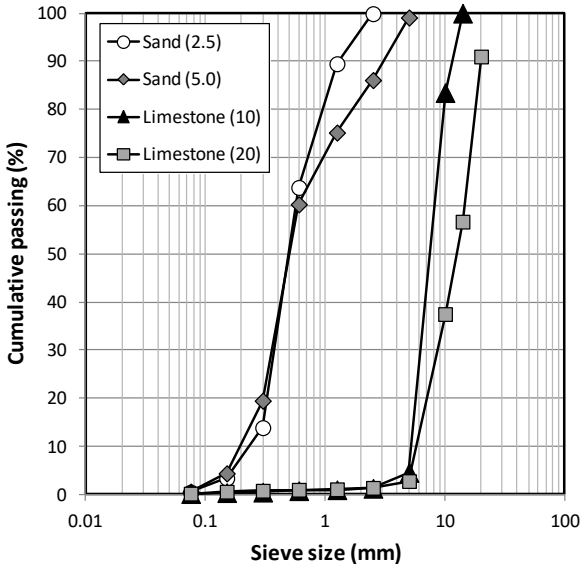

Fig. 1 Particle size distribution of fine and coarse aggregates.

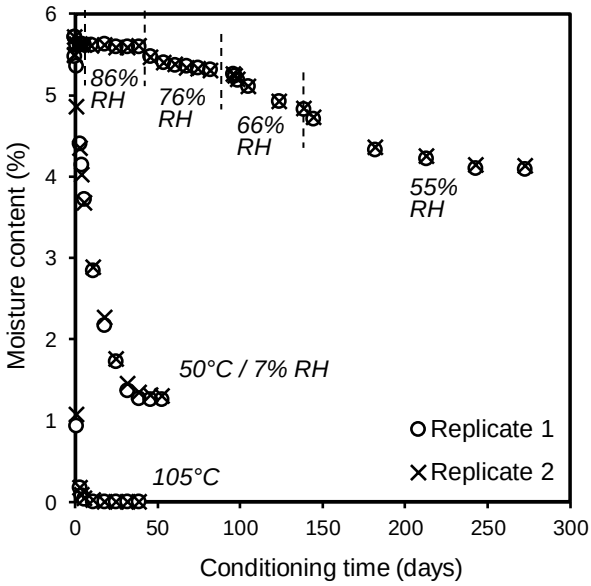

Fig. 2 Example plot showing change in moisture content with conditioning time when dried at 105°C, 50°C/7% RH, or 21°C stepwise from 93% RH → 55% RH for two replicate samples of C10: 50 (28d).

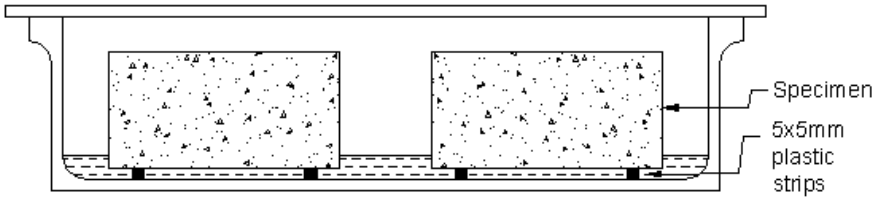

Fig. 3 Schematic of the test set-up for capillary absorption (sorptivity).

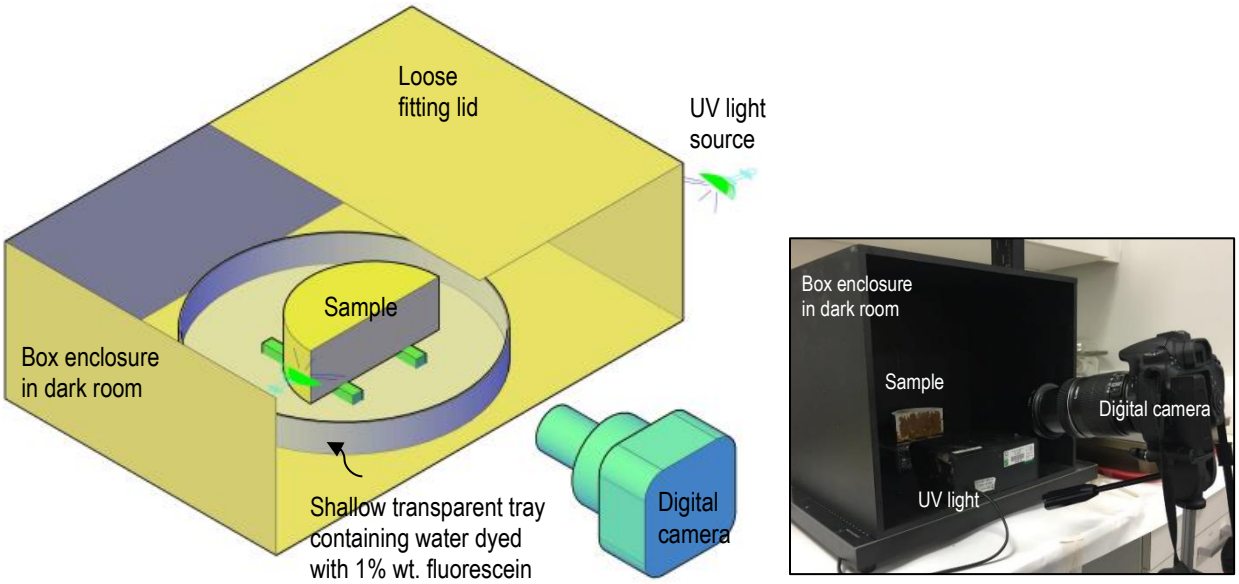

Fig. 4 Set-up for fluorescence imaging of water penetration front during capillary absorption.

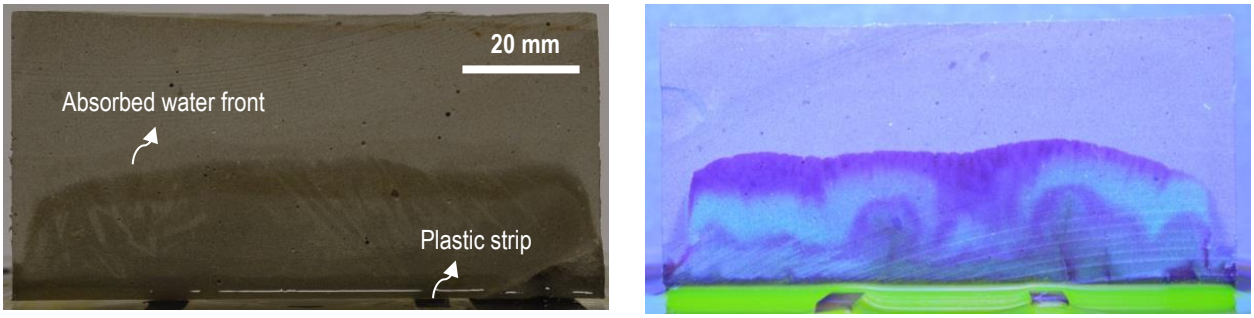

a) Water

b) Water + 1% wt. fluorescein

Fig. 5 Example images showing depth of water penetration after two hours of capillary absorption in (a) water and (b) water containing 1% wt. fluorescein, illuminated with UV light.

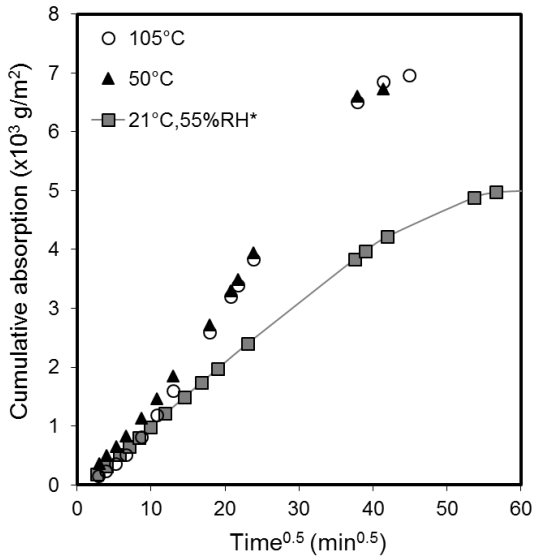

a) C20:50 (t/MSA = 2.5)

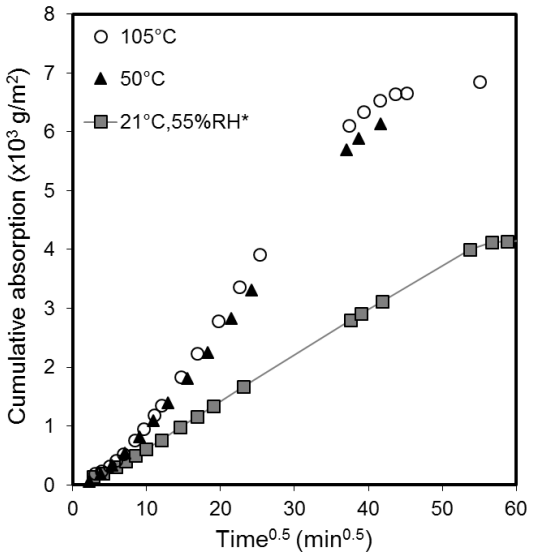

b) C10:50 (t/MSA = 5)

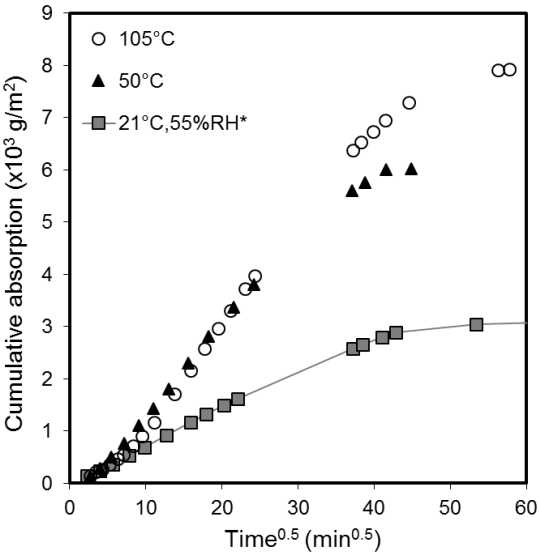

c) M5:50 (t/MSA = 10)

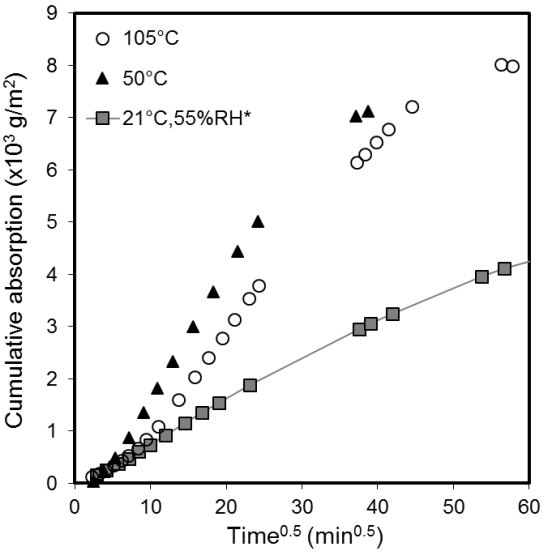

d) M2.5:50 (t/MSA = 20)

Fig. 6 Examples of cumulative water absorption plots for 50 mm thick concrete and mortar discs at various t/MSA ratio and conditioning regimes. Some samples displayed significant departure from the expected linearity between cumulative absorption and square root time.

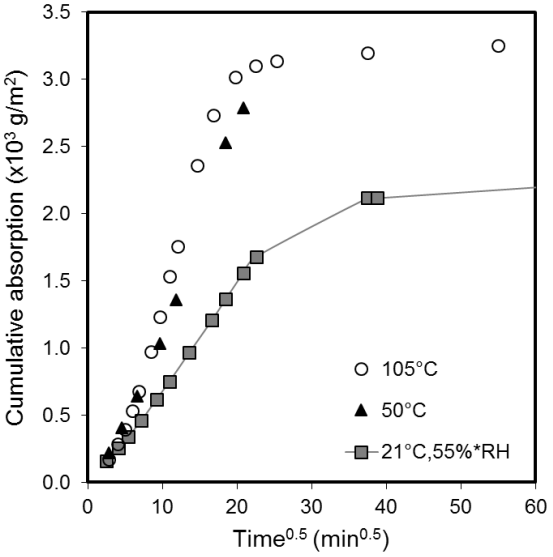

a) C10:25 (t/MSA = 2.5)

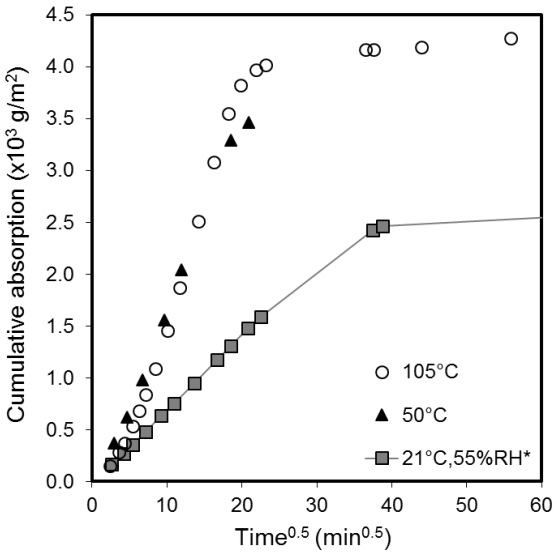

b) M5:25 (t/MSA = 5)

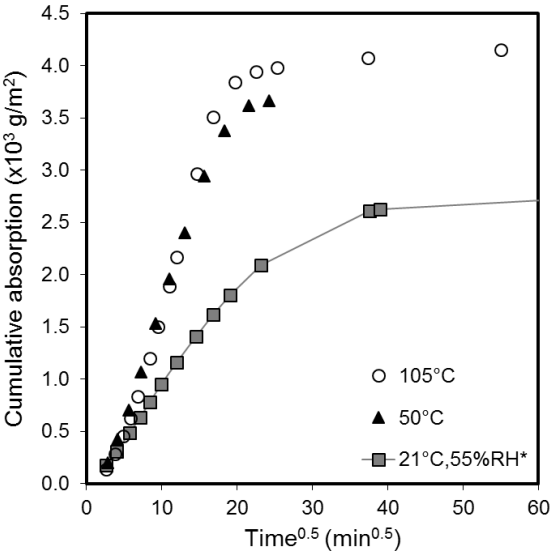

c) M2.5:25 (t/MSA = 10)

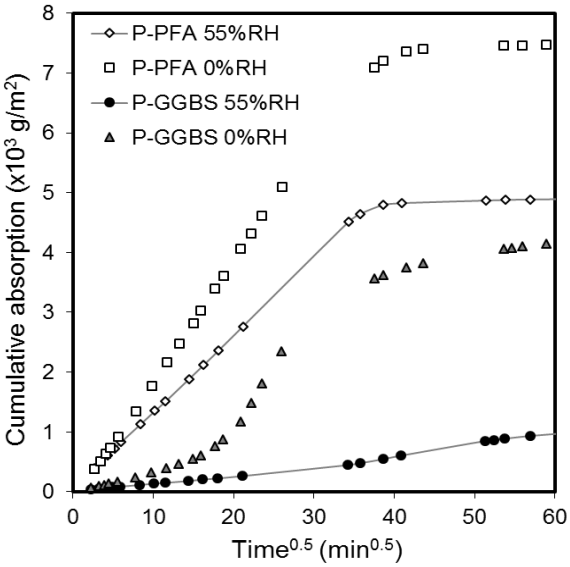

d) P-GGBS & P-PFA

Fig. 7 Examples of cumulative water absorption plots for 20-25 mm thick concrete, mortar and paste discs at various t/MSA ratio and conditioning regimes. Some samples displayed significant departure from the expected linearity between cumulative absorption and square root time.

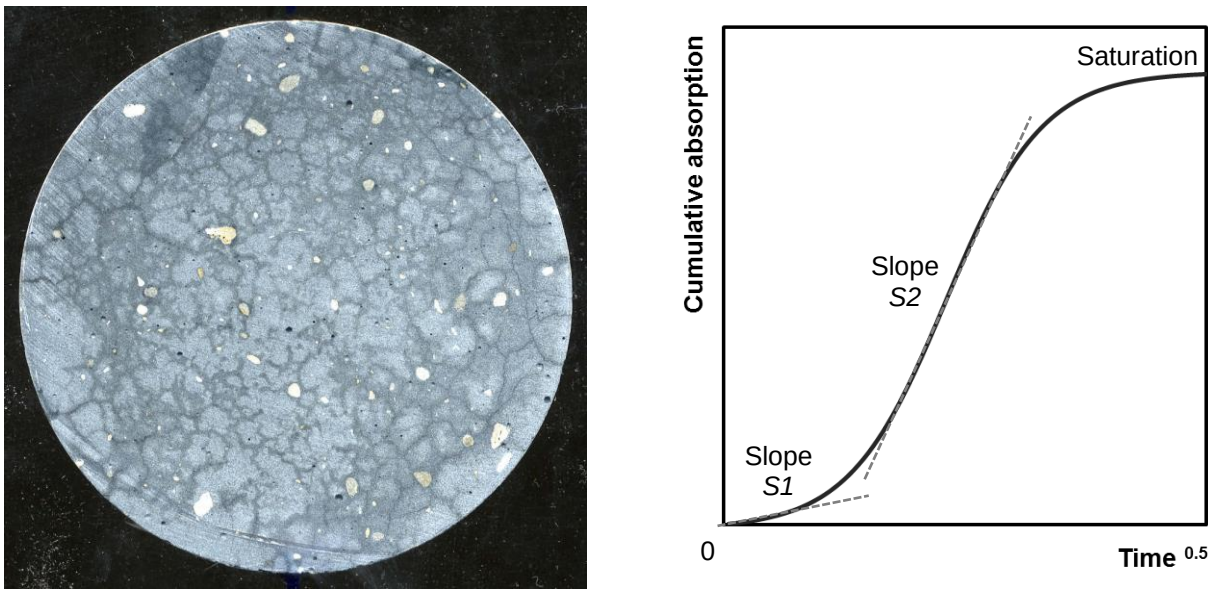

(a) (b)

Fig. 8 a) Some samples showed map crack pattern on top surface during water absorption testing that coincided with the inflection point on the cumulative plot; b) Determination of *S1* and *S2* from the cumulative absorption plot to highlight the absorption anomaly.

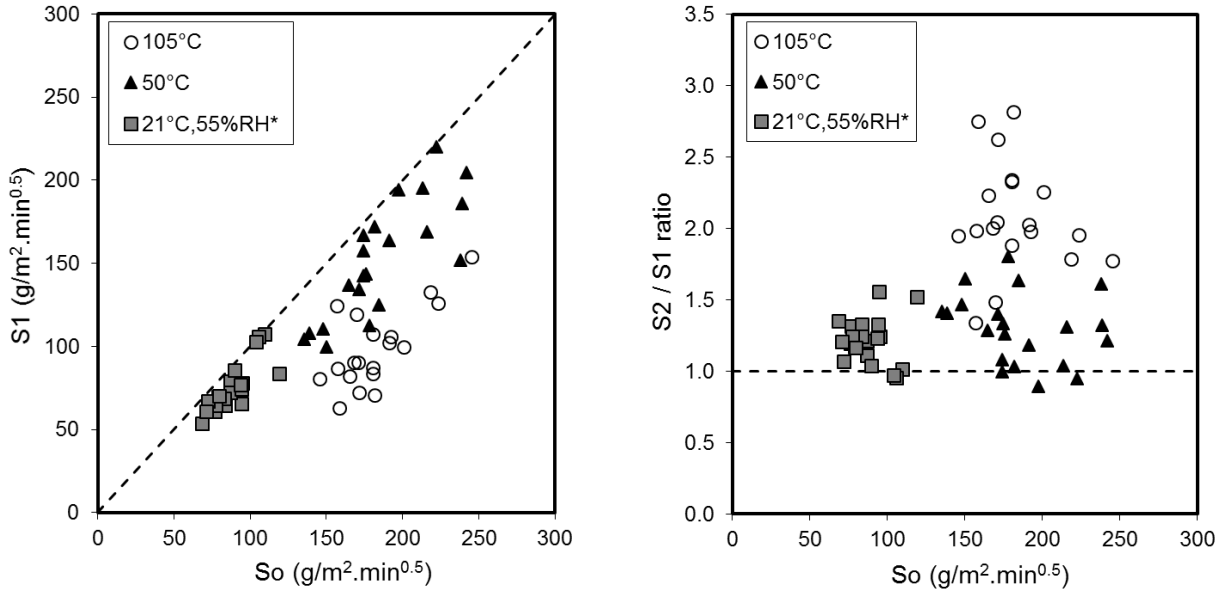

a) b)

Fig. 9 Scatter plots showing the effect of drying on the relationships between S_O, S1 and S2: a) S1 against S_O, and b) S2/S1 against S_O. The extent of anomalous behaviour increases with severity of drying. Data are from mortar and concrete samples.

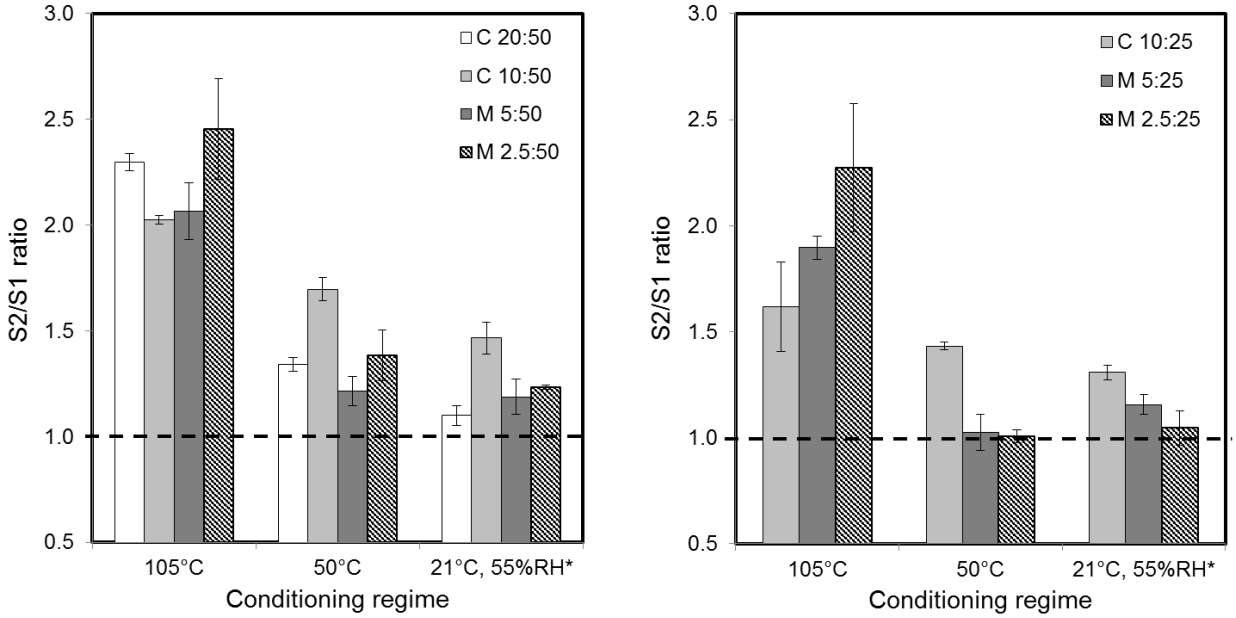

a) t = 50 mm b) t = 25 mm

Fig. 10 Average S2/S1 sorptivity ratio measured on 50 mm and 25 mm thick discs subjected to different drying regimes. The extent of the anomalous behaviour increases with severity of drying.

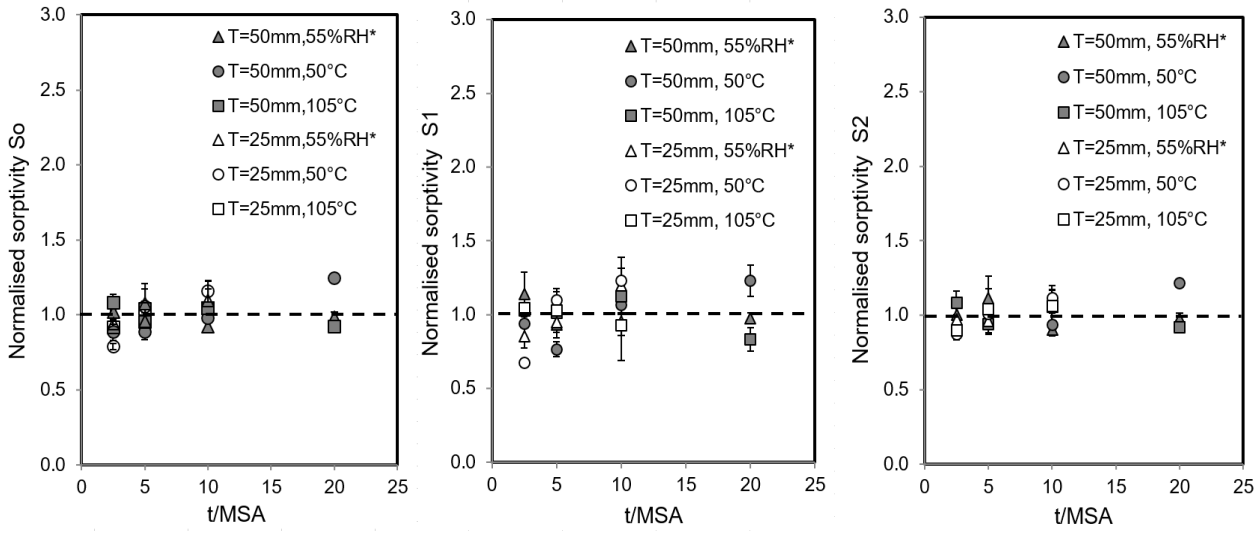

Fig. 11 Effect of t/MSA ratio on the sorptivity coefficients So, S1 and S2 of mortars and concretes with different conditioning regimes.

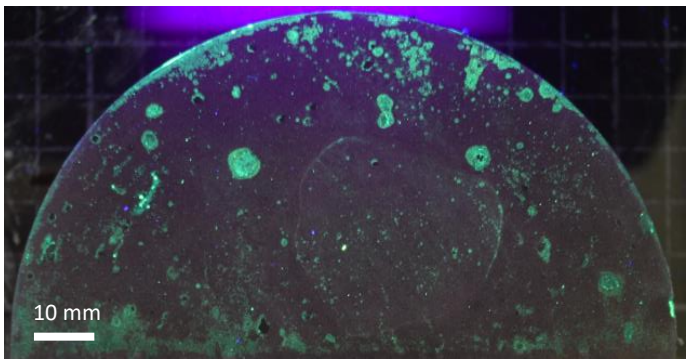

a) 21°C, 55% RH*

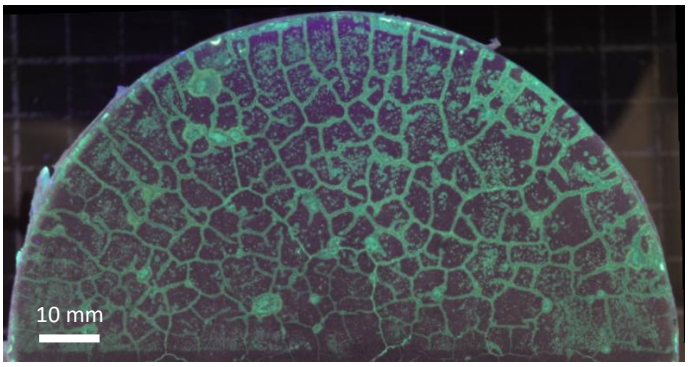

b) 50˚C, 7% RH

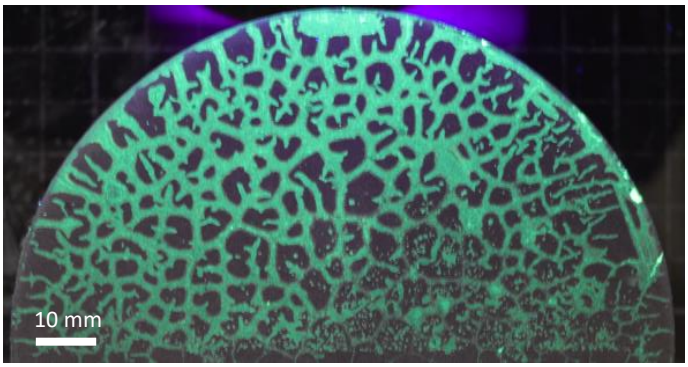

c) 105 ˚C

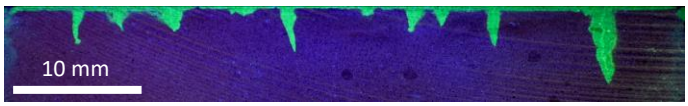

d) 105 ˚C

Fig. 12 Fluorescence imaging showing microcracking on the exposed surface (a, b, c) and cross-section (d) of samples subjected to stepwise drying at 21°C, 55%RH, oven drying at 50°C, 7%RH and oven drying at 105°C.

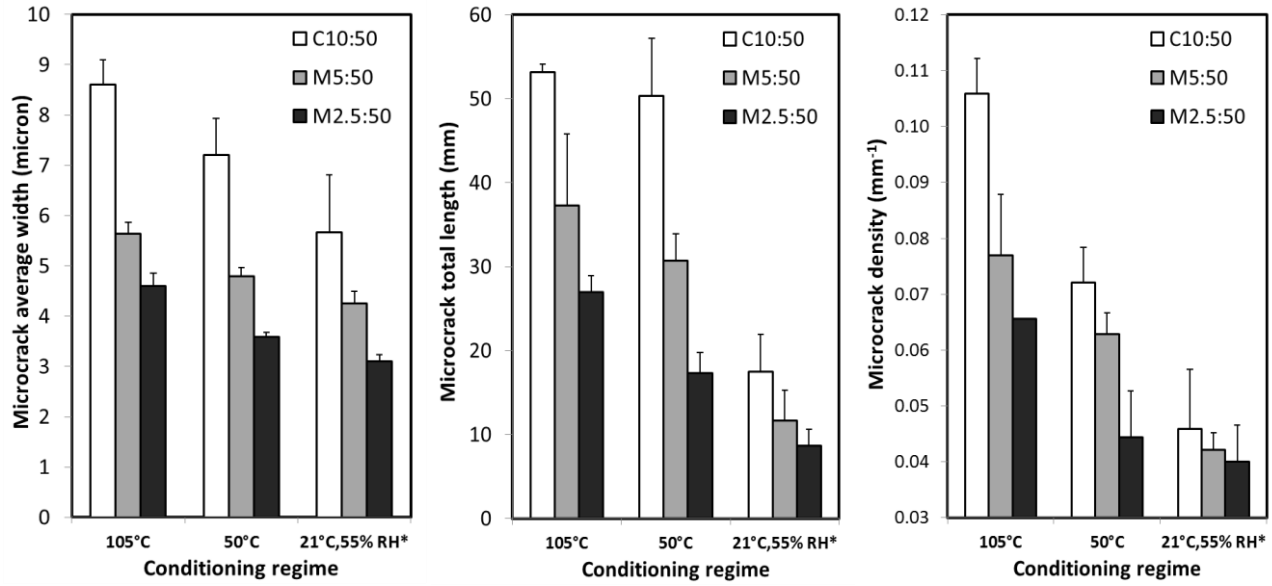

a) Average width a) Total length c) Density

Fig. 13 Effect of drying regime on the width, length and density of microcracks measured on cross-section of samples by image analysis of fluorescence microscopy images.

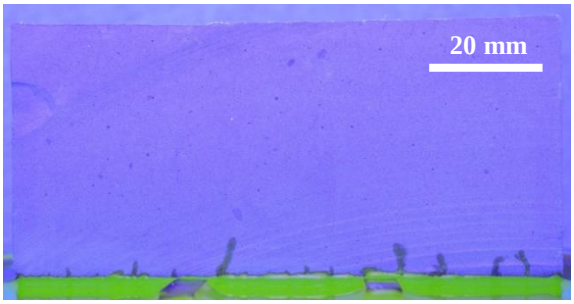

a) 9 sec

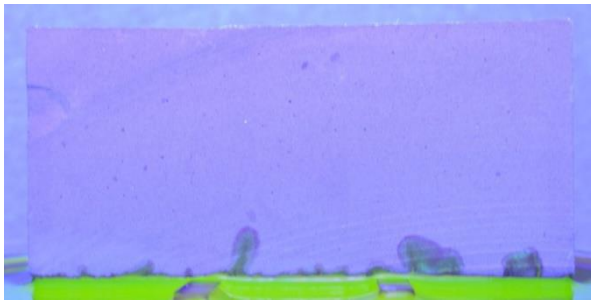

b) 2 min, 18 sec

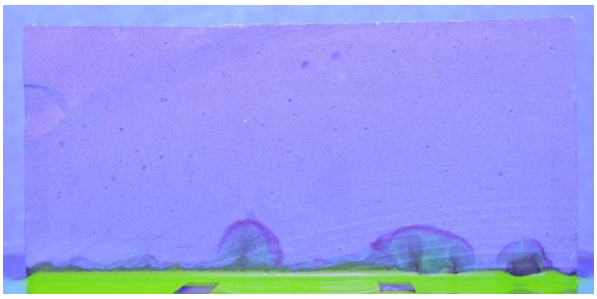

c) 20 min, 5 sec

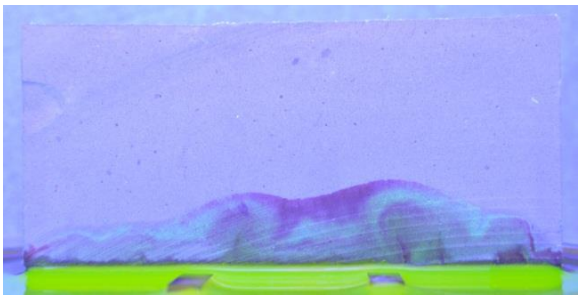

d) 65 min, 29 sec

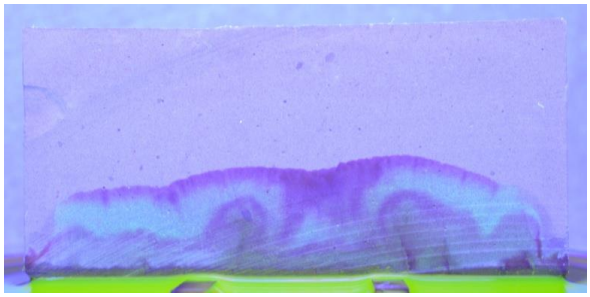

e) 1hr, 45 min, 26 sec

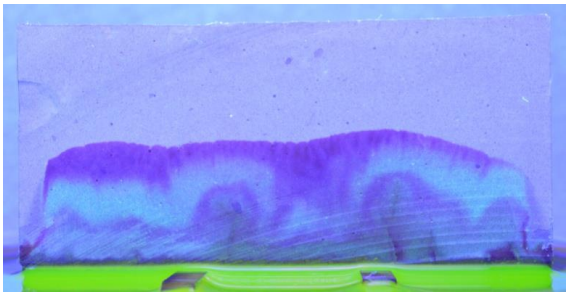

f) 2 hrs, 15 min, 31 sec

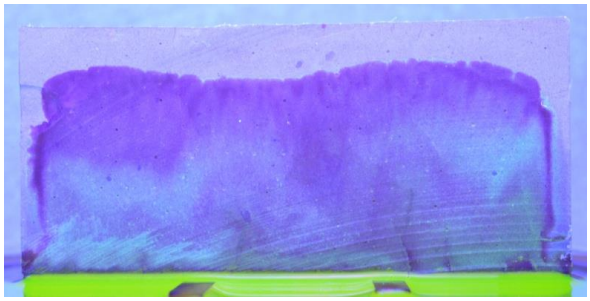

g) 4 hrs, 46 min, 8 sec

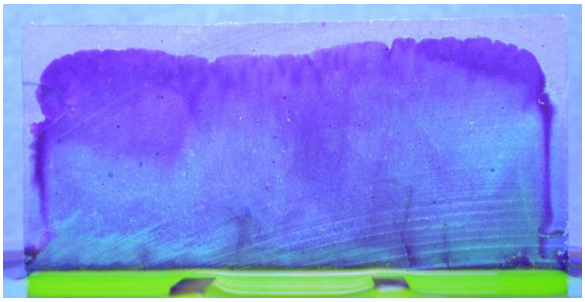

h) 5 hrs, 42 min, 20 sec

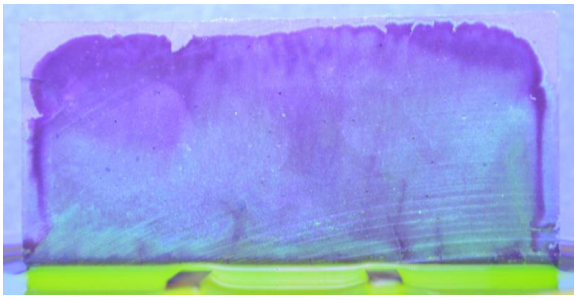

i) 6 hrs, 43 min, 34 sec

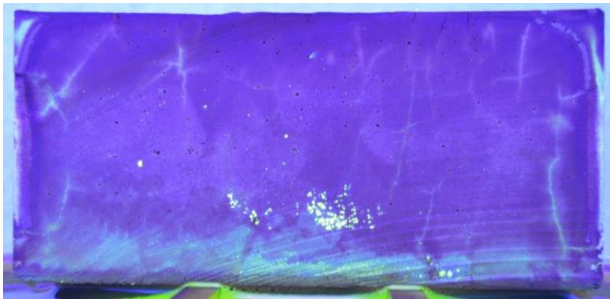

j) 23 hrs

Fig. 14 Fluorescence images showing water penetration by capillary absorption in a paste conditioned at 50°C, 7%RH. Initial uptake is dominated by rapid absorption into the drying-induced microcracks

at the surface region, producing a highly irregular penetration front. Subsequent uptake occurs via non-cracked regions and the effect of microcracks diminishes.

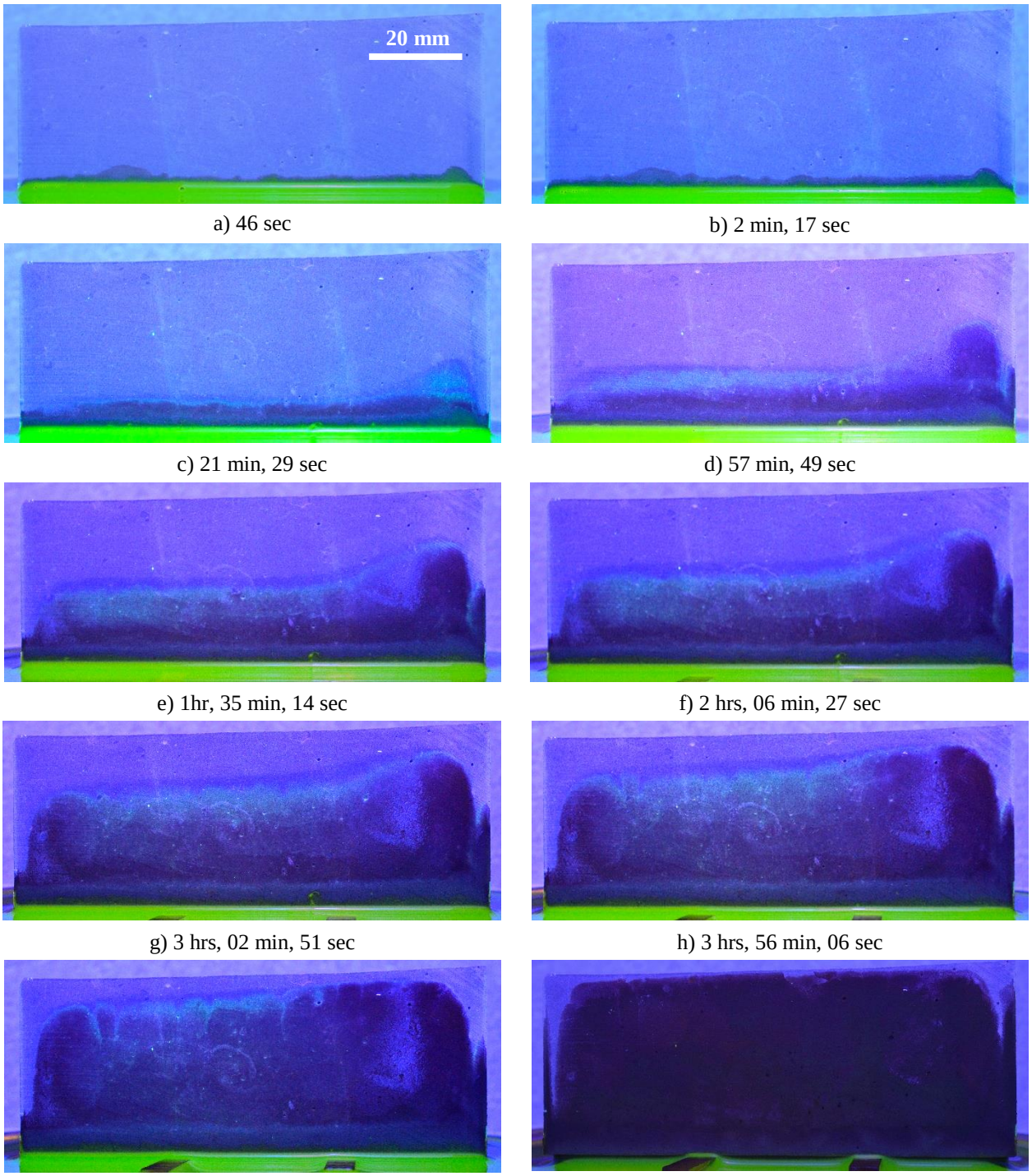

a) 46 sec

b) 2 min, 17 sec

c) 21 min, 29 sec

d) 57 min, 49 sec

e) 1hr, 35 min, 14 sec

f) 2 hrs, 06 min, 27 sec

g) 3 hrs, 02 min, 51 sec

h) 3 hrs, 56 min, 06 sec

i) 4 hrs, 43 min, 19 sec

j) 22 hrs

Fig. 15 Fluorescence images showing water penetration by capillary absorption in a paste conditioned by gentle step-wise drying at 21°C, 55%RH*. Water uptake is less affected by surface microcracking and the penetration front is more regular compared to severely dried samples (Fig. 13).

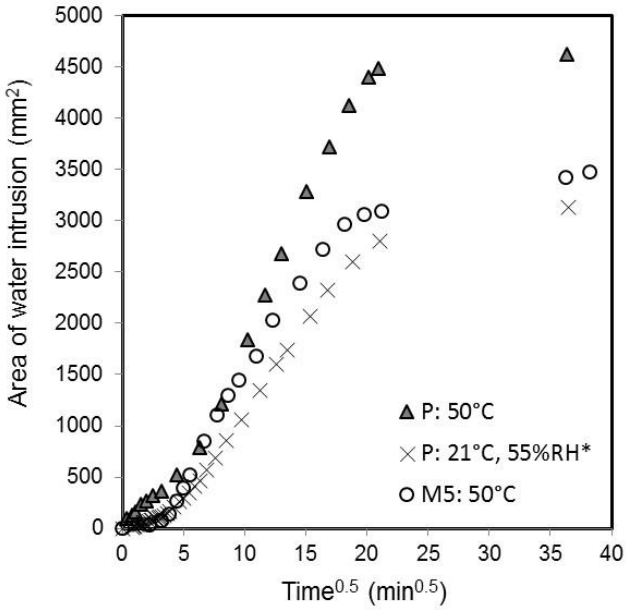

Fig. 16 Cumulative area of water intrusion showing non-linear absorption in agreement with gravimetric measurement. Data were obtained from image analysis on fluorescence images.